Research Square

Preprints are preliminary reports that have not undergone peer review.
They should not be considered conclusive, used to inform clinical practice,
or referenced by the media as validated information.

Regional Ocean Conditions Shape Mesoscale Eddy Thermal Responses to ENSO Diversity in the Subtropical Southeastern Indian Ocean

Chen Fang

fangchen@fio.org.cn

First Institute of Oceanography Ministry of Natural Resources https://orcid.org/0009-0003-1794-5326

Guang Yang

First Institute of Oceanography Ministry of Natural Resources https://orcid.org/0000-0001-8365-8147

Lin Liu

First Institute of Oceanography Ministry of Natural Resources

Xia Zhao

First Institute of Oceanography Ministry of Natural Resources

Research Article

Keywords: EP and CP ENSO, Southeastern Indian Ocean, Mesoscale eddies, Vertical thermal structure, Subsurface cold cores, Vertical shear, Westward eddy propagation

Posted Date: November 14th, 2026

DOI: https://doi.org/10.21203/rs.3.rs-11440723/v1

License: This work is licensed under a Creative Commons Attribution 4.0 International License.
Read Full License

Regional Ocean Conditions Shape Mesoscale Eddy Thermal Responses to ENSO Diversity in the Subtropical Southeastern Indian Ocean

Chen Fang[1, 2], Guang Yang[1, 2*], Lin Liu[1, 2], Xia Zhao[2, 3]

1 Center for Ocean and Climate Research, First Institute of Oceanography, Ministry of Natural Resources, Qingdao, China

2 Shandong Key Laboratory of Marine Science and Numerical Modeling, Qingdao, China

3 Key Laboratory of Marine Science and Numerical Modeling, First Institute of Oceanography, Ministry of Natural Resources, Qingdao, China

*Corresponding author: *Dr. Guang Yang, First Institute of Oceanography, Ministry of Natural Resources, Qingdao 266061, China. Email: gyang@fio.org.cn*

Abstract

Satellite altimetry, Argo profiles, and ocean reanalysis are used to examine mesoscale eddy thermal responses to eastern-Pacific (EP) and central-Pacific (CP) ENSO in the subtropical southeastern Indian Ocean. Anticyclonic temperature anomalies relative to climatology broadly follow regional background changes. During EP-El Niño, eastern subsurface cooling and central shallow warming coincide with weaker eastern but strong central warm-core anomalies. Leeuwin Current variations suggest that changes in poleward warm-water transport contribute to the eastern temperature response. Cyclonic eddies retain subsurface cold cores under all four ENSO conditions, with pronounced upper-ocean warming producing a warm-over-cold structure during CP-La Niña. Subtracting matched contemporaneous out-of-eddy temperatures preserves these cores and their greater depth in the central sector. The ENSO–shear relationship is stronger for meridional than zonal shear in the eastern Leeuwin Current–Leeuwin Undercurrent system, whereas zonal shear in the central South Indian Countercurrent–South Equatorial Current system is associated with both ENSO indices. These shear changes may affect eddy development through baroclinic instability. Approximately 15–17% of eastern-origin eddies propagate into the central sector and may retain thermal properties acquired upstream. Regional background temperature thus helps explain anticyclonic thermal contrasts, while circulation adjustments and westward propagation may also contribute to subsurface thermal variability.

Keywords: EP and CP ENSO, Southeastern Indian Ocean, Mesoscale eddies, Vertical thermal structure, Subsurface cold cores, Vertical shear, Westward eddy propagation.

1 Introduction

Mesoscale eddies are a major source of ocean variability because they redistribute momentum, heat, salt, and biogeochemical tracers across a broad range of horizontal and vertical scales (Chelton et al. 2011). Their thermohaline signatures are therefore central to understanding how the upper ocean responds to climate variability and remote forcing. At the sea surface, eddy-induced temperature anomalies also exhibit diverse spatial patterns, with dipole structures making a substantial contribution to their global variance(Lv et al. 2026). Composite analyses combining

satellite altimetry and Argo profiles further show that mesoscale eddies can exhibit vertically distinct thermohaline structures (Chaigneau et al. 2011). Together, these studies provide an observational basis for linking mesoscale eddies to upper-ocean thermohaline variability. Observations in the southeastern tropical Indian Ocean have linked energetic mesoscale variability to heat and salt transport and chlorophyll redistribution. Satellite and Argo measurements have also resolved the vertical structure of these eddies, including intrathermocline features, and documented seasonal changes in their intensity (Ding et al., 2026; Liu et al., 2023; Yang et al., 2015, 2019; Zu et al., 2022).

Compared with the tropical southeastern Indian Ocean, the Subtropical Southeastern Indian Ocean (SSIO) has been studied more extensively in terms of eddy kinetic energy (EKE) than individual eddy vertical structure. The regional circulation is shaped by the South Equatorial Current (SEC), South Indian Countercurrent (SICC), Leeuwin Current (LC), and Leeuwin Undercurrent (LUC). The SICC occupies the upper several hundred meters between approximately 20°S and 30°S, whereas the SEC contributes westward flow and vertical shear in the basin interior (Menezes et al. 2014, 2016). Along the eastern boundary, the LC responds to pressure gradients and interannual sea level variability, and its strength is closely linked to ENSO (Feng et al. 2003; Li and Clarke 2004; Zheng et al. 2018; Zhang et al. 2020). This dynamical setting suggests that eddies in the SSIO may exhibit pronounced regional contrasts in vertical thermal structure rather than a spatially uniform response across the basin.

Pacific ENSO variability reaches the southern Indian Ocean through oceanic connections involving the Indonesian Throughflow and the western Australian coastal waveguide. The resulting coastal sea level and LC adjustments can be accompanied by baroclinic Rossby waves carrying the signal westward into the basin interior (Potemra 2001; Feng et al. 2003; Delman et al. 2018; Zheng et al. 2018; Zhang et al. 2020; Zhu et al. 2025). At mesoscale, the enhanced activity observed in the LC–SICC system during La Niña links regional EKE variability to tropical Pacific forcing (Zheng et al. 2018; Zhang et al. 2020). Whether this connection also entails ENSO-type-dependent changes in the vertical thermal structure of cyclonic and anticyclonic eddies remains unresolved.

The distinction between eastern Pacific (EP) and central Pacific (CP) ENSO involves both the spatial distribution of sea surface temperature anomalies and the evolution of individual events. Differences in remote impacts also depend on the asymmetry between the warm and cold phases

(Ashok et al. 2007; Kao and Yu 2009; Ren and Jin 2011; Takahashi et al. 2011; Yu et al. 2011; Wang and Wang 2014; Ren and Wang 2020; Wang and Li 2022; Li et al. 2024; Nguyen-Le et al. 2024). For the Indian Ocean, this diversity is expressed through variations in thermocline conditions and sea level, together with adjustments of the large-scale atmospheric circulation (Eabry et al., 2021; Jo et al., 2022; Yang et al., 2019). Previous studies have further demonstrated that ENSO and the South China Sea summer monsoon exert distinct and interacting influences on Indian Ocean Dipole (IOD) variability, involving large-scale atmospheric circulation adjustments and regional air–sea feedbacks (Zhang et al. 2021, 2024, 2025).These findings motivate a specific question for the SSIO: Do EP-El Niño, EP-La Niña, CP-El Niño, and CP-La Niña produce distinct vertical thermal responses within mesoscale eddies, and do those responses vary systematically from the eastern boundary to the western interior?

Within the SSIO eddy corridor, propagating eddies can preserve distinct water-mass properties, with both surface- and subsurface-intensified structures represented in the regional population (Dilmahamod et al. 2018). The comparison by Ding et al. (2026) showed that these two groups differ in longevity and displacement as well as in three-dimensional structure and meridional heat transport. Their findings give particular importance to subsurface-intensified cyclonic eddies in regional heat redistribution and indicate that transport assessments must account for both vertical structure and internal asymmetry. This structural and transport perspective provides a basis for examining how the regional eddy field varies with climate conditions.

Building on this framework, we approach eddy vertical structure from a complementary climate-variability perspective. Rather than separating eddies according to whether they are surface- or subsurface-intensified, we ask how the three-dimensional thermal anomalies within cyclonic and anticyclonic eddies vary under different large-scale climate states. Specifically, it remains unclear whether EP and CP ENSO events modify the vertical expression of eddy thermal anomalies in the same way, and whether such responses differ between the Leeuwin Current–Leeuwin Undercurrent system near the eastern boundary and the offshore South Indian Countercurrent–South Equatorial Current system.

This study focuses on two adjoining sectors of the subtropical southeastern Indian Ocean: an eastern sector, R1 (105°-115°E, 20°-35°S), and a central sector, R2 (85°-105°E, 20°-35°S). Section 2 describes the data sets, eddy identification and tracking, Argo-eddy collocation, and ENSO classification. Section 3 first characterizes ENSO-related background thermal and

circulation conditions, then examines ENSO-leading variability in regional eddy activity and the three-dimensional thermal structures of anticyclonic and cyclonic eddies. It further assesses eddy-induced thermal anomalies relative to matched contemporaneous out-of-eddy environmental (OE) profiles before evaluating the relationships between eddy thermal structure, local background temperature, regional vertical shear, and westward eddy propagation. Section 4 summarizes the principal findings, discusses their physical interpretation and regional implications, and outlines the main limitations of the analysis.

2 Data and Methods

2.1 Study Region and Data Sets

The study area is located in the subtropical southeastern Indian Ocean (SSIO; 20°-35°S). The detailed eddy-Argo analysis focuses on Region 1 (R1; 105°-115°E) and Region 2 (R2; 85°-105°E), which together form an eastern-to-central corridor across the SSIO.

Eddy identification, tracking, and eddy kinetic energy (EKE) calculations used daily sea level anomaly (SLA) and geostrophic velocity fields from the delayed-time, multi-mission gridded sea level product distributed by the Copernicus Marine Service (Copernicus Marine Service 2025). The fields cover January 1993 to December 2025 on a 0.25° × 0.25° horizontal grid. Here, u' and v' denote anomalous zonal and meridional geostrophic velocities, respectively.

$$EKE = \frac{1}{2}(u'^2 + v'^2)$$

Argo temperature profiles for January 2000 to December 2025 were obtained from the Argo Global Data Assembly Centre. Only profiles passing standard Argo quality-control criteria were retained. Monthly climatological temperature fields from the 1991–2020 climate-normal product of World Ocean Atlas 2023 (WOA23) were used to calculate climatology-referenced anomalies (National Centers For Environmental Information 2024). Monthly temperature and horizontal velocity fields used for background-state diagnostics were obtained from the NOAA/NCEP Global Ocean Data Assimilation System (GODAS) for January 1993 to December 2025 (Behringer and Xue 2004) and analyzed on a 2.5° × 2.5° grid. Monthly SST from NOAA ERSSTv5 over the same period was used to construct the Niño-3.4, EP, and CP ENSO indices (Huang et al. 2017).

Figure 1a shows that the study corridor lies within a zonally elongated band of enhanced high-pass SSH variability that is strongest near the eastern boundary and extends westward into R2, indicating pronounced mesoscale activity in both regions.

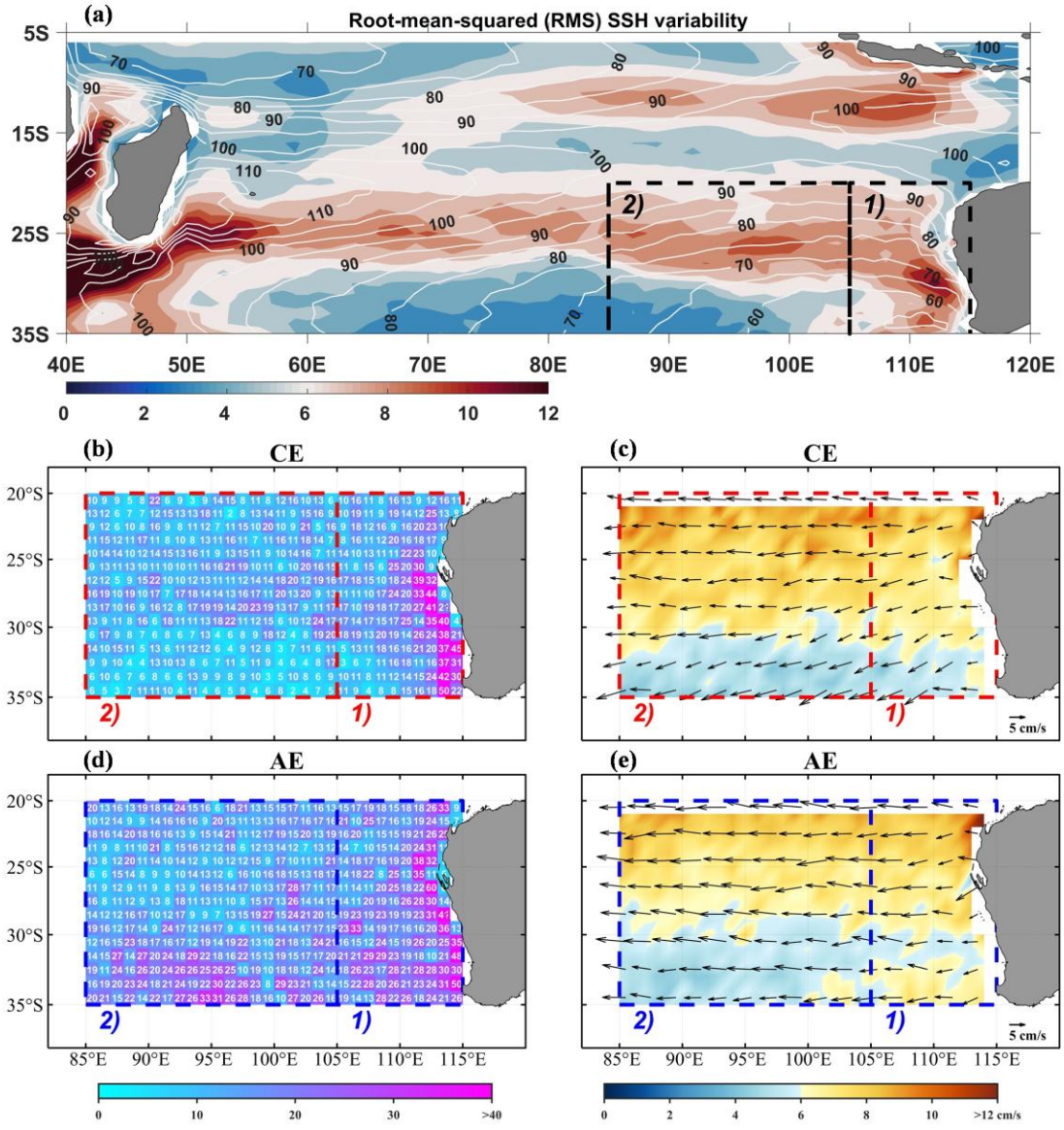


Figure 1. (a) Root-mean-square (RMS) variability of high-pass-filtered sea surface height (SSH), with shading in centimeters. White contours denote the background SSH field, and the black dashed boxes delineate Region 1 (R1; 105°-115°E, 20°-35°S) and Region 2 (R2; 85°-105°E, 20°-35°S). The zonally elongated band of elevated high-pass SSH variability extending westward from the eastern boundary into R2 indicates enhanced mesoscale eddy activity in both

R1 and R2. (b, d) Spatial distributions of newly generated cyclonic eddies (CEs) and anticyclonic eddies (AEs), respectively, during 1993–2025. The numbers indicate the number of newly generated eddies within each 1° × 1° grid cell, while the color shading represents their spatial density. (c, e) Climatological annual-mean translation velocity fields of CEs and AEs, respectively. Eddy translation velocities were calculated using a forward-difference scheme based on the daily displacement of the eddy centroid. Arrows indicate normalized propagation direction, and shading represents propagation speed (cm s^{-1}). The red and blue dashed boxes delineate R1 and R2 in the CE and AE panels, respectively.

2.2 Eddy Identification, Tracking, and Statistical Samples

Mesoscale eddies were identified from SLA using the winding-angle method (Ari Sadarjoen and Post 2000). The implementation follows Chaigneau et al. (2008) and Chaigneau et al. (2009). In the Southern Hemisphere, counterclockwise and clockwise closed streamlines were classified as AEs and CEs, respectively. Eddies were linked between consecutive time steps using their positions, sizes, and boundary continuity. Only eddies with lifetimes of at least 21 days were retained. Yang et al. (2015) used the same method to characterize mesoscale eddies and their vertical structure and associated heat and salt transports in the southeastern tropical Indian Ocean. From January 1993 to December 2025, 2,960 AEs and 2,419 CEs were identified in R1, and 4,731 AEs and 3,345 CEs were identified in R2 (Figures 1b and 1d). Both CEs and AEs propagate predominantly westward across the study region (Figures 1c and 1e), consistent with the prevailing westward propagation of mesoscale eddies in the southeastern Indian Ocean. Translation speed exhibits a pronounced meridional dependence, with faster propagation in the northern part of the study region and progressively slower propagation toward the south. Relatively high speeds also occur near the eastern boundary in R1, whereas eddies propagate more slowly in the southern portions of both regions. Despite their opposite polarities, CEs and AEs exhibit broadly similar spatial patterns of propagation direction and translation speed.

2.3 Argo-Eddy Collocation and Composite Construction

Argo profiles were collocated with the contemporaneous eddy field by observation time and position. Profiles inside eddy boundaries were classified as in-eddy profiles, whereas profiles outside eddy boundaries were retained as OE profiles. Profile positions were normalized by eddy-center position and effective radius before compositing. The R1 data set contains 1,076 in-CE

profiles, 839 in-AE profiles, and 8,154 OE profiles; R2 contains 1,469 in-CE profiles, 1,689 in-AE profiles, and 17,443 OE profiles. Figure 2 shows that the collocated observations sample both eddy cores and peripheral locations.

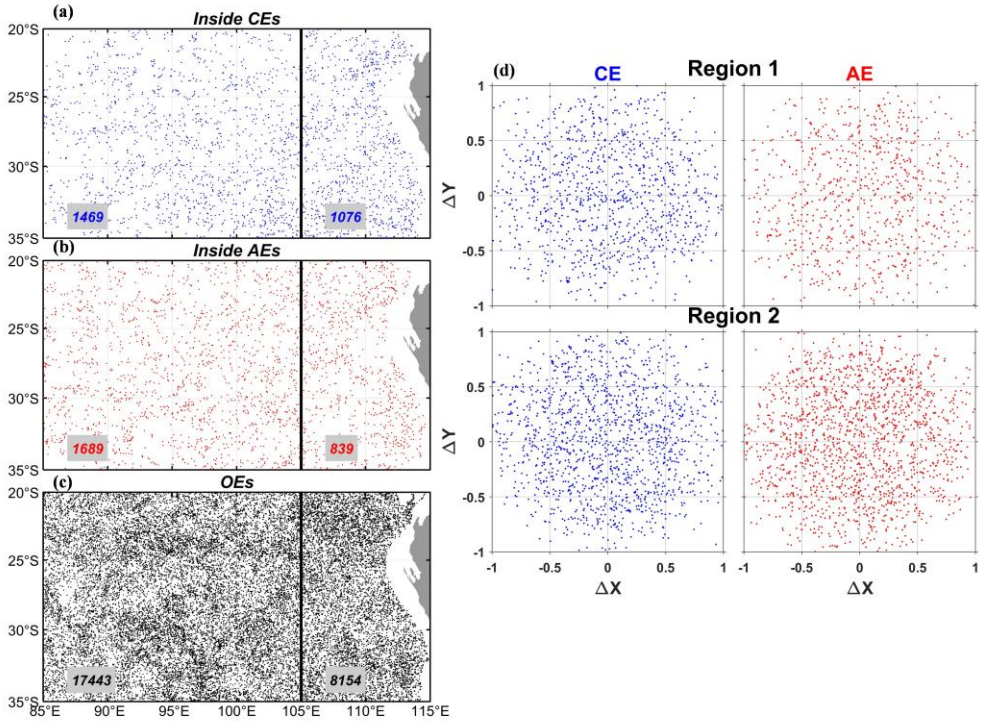


Figure 2. (a–c) Geographic distributions of Argo profiles located within CEs, within AEs, and outside eddies (OEs), respectively. Blue, red, and black dots represent individual Argo profiles associated with CEs, AEs, and OEs, respectively. The black vertical line at 105°E separates Region 2 (R2; 85°-105°E, 20°-35°S) from Region 1 (R1; 105°-115°E, 20°-35°S), and the numbers indicate the total number of Argo profiles in each region. (d) Distributions of Argo profiles within CEs (blue) and AEs (red) in the normalized eddy-coordinate space (ΔX, ΔY) for R1 (upper panels) and R2 (lower panels). Each dot represents the normalized position of an individual Argo profile relative to the corresponding eddy center.

WOA23-referenced temperature anomalies include both eddy-associated perturbations and environmental departures from the 1991–2020 climatology, which encompasses ENSO and non-ENSO years. To estimate eddy-induced anomalies relative to the contemporaneous background, we subtract matched out-of-eddy environmental (OE) profiles from in-eddy profiles, adapting the approach of Schütte et al. (2016).

For each in-eddy Argo profile, OE profiles within the same ENSO category are searched sequentially using three time–distance windows: ±7 days/200 km, ±14 days/150 km, and ±28

days/100 km. Both temporal and spatial separations are measured between the in-eddy and OE Argo profiles. In-eddy profiles are grouped into three radial zones: 0-1/3R, 1/3-2/3R, and 2/3-1R, where R is the eddy radius. Within each region, ENSO category, and eddy polarity, zone-mean in-eddy temperatures and their matched OE references are combined using area weights of 1/9, 3/9, and 5/9. Their difference defines the composite eddy-induced potential-temperature anomaly.

2.4 ENSO Classification and Composite Periods

The evolution of the Niño-3.4, EP, and CP indices calculated from NOAA ERSSTv5 was used to classify ENSO events (Figure 3). To distinguish the EP and CP components, we applied the transformation of Ren & Jin (2011) to the monthly Niño-3 (N3) and Niño-4 (N4) sea surface temperature anomaly (SSTA) indices:

$$\begin{cases} N_{\mathrm{CT}} = N_3 - \alpha N_4, \\ N_{\mathrm{WP}} = N_4 - \alpha N_3, \end{cases} \quad where\ \alpha = \begin{cases} \frac{2}{5}, & N_3 N_4 > 0, \\ 0, & \text{otherwise.} \end{cases}$$

Here, N_{CT} and N_{WP} denote the cold-tongue and warm-pool Niño indices, referred to here as the EP and CP indices, respectively. This phase-dependent transformation removes the component shared by the Niño-3 and Niño-4 anomalies and emphasizes their relative eastern- and central-Pacific signals. Because Argo observations begin in 2000, the Argo-based eddy composites include only ENSO events occurring during 2000–2025.

The Argo composite analysis includes CP-El Niño events in 2002, 2004, 2009, and 2018; EP-El Niño events in 2006, 2015, and 2023; CP-La Niña events in 2000, 2010, 2011, 2020, and 2021; and EP-La Niña events in 2005, 2007, and 2017.

Figure 3 shows that the selected events are characterized by distinct positive or negative EP and CP index anomalies, providing a consistent basis for separating responses by ENSO type and phase. Earlier events, such as the 1997/98 EP El Niño, were retained in the SLA-based eddy statistics where applicable but excluded from the Argo composite analysis because Argo sampling was insufficient.

We used a common DJF(0)–SON(1) window for the seasonal background composites and the Argo-based three-dimensional eddy composites in Figures 9 and 10. The labels 0 and 1 identify the ENSO developing year and the following year. For each selected event, Argo profiles were composited within this window according to ENSO category.

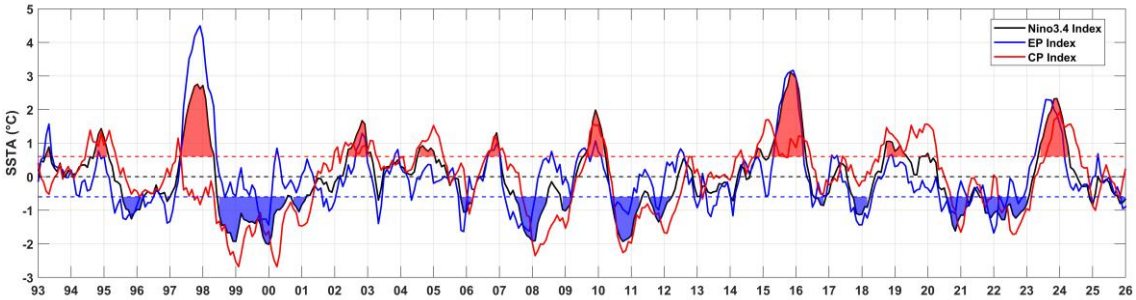


Figure 3. Time series of ENSO indices from January 1993 to December 2025. The Niño-3.4 index (black), eastern Pacific (EP) index (blue), and central Pacific (CP) index (red) were calculated from monthly SSTA derived from ERSSTv5. The red and blue shaded areas denote El Niño and La Niña events, respectively, identified as periods when the corresponding ENSO index remains above +0.5 or below −0.5 standard deviations for at least three consecutive months. The horizontal dashed lines indicate the ±0.5-standard-deviation thresholds used for ENSO event identification.

3 Results

3.1 ENSO-Related Background Thermal Structure and Circulation

Longitude–pressure sections reveal pronounced regional and vertical differences in the subsurface thermal response to the four ENSO conditions (Figure 4). Generally, the remarkable anomalies occur during both CP-La Niña and EP-El Niño, whereas the responses during CP-El Niño (EP-La Niña) are relatively weaker and less spatially coherent compared with the EP-El Niño (CP-La Niña).

During CP-La Niña, strong positive temperature anomalies persist in R1 throughout the whole year. In DJF(0) and MAM(1), the warming extends from the near surface to approximately 300–400 dbar and is strongest near the eastern boundary. Positive anomalies are also evident farther west in R2, mainly at approximately 100–300 dbar, and become more spatially continuous during JJA(1) and SON(1). The subsurface response therefore indicates a persistent warm anomaly extending westward from R1 into eastern R2. EP-El Niño exhibits a markedly different vertical structure. Pronounced negative temperature anomalies occur in R1, primarily at approximately 100–400 dbar, and are strongest during DJF(0) and MAM(1). The cooling remains evident during JJA(1) but weakens considerably by SON(1). In contrast, shallow positive anomalies occur farther west, mainly within R2 during the early stages of the event. EP-El Niño therefore produces a pronounced east–west and vertical contrast, with subsurface cooling in R1 and shallower warming

farther west. The other two ENSO conditions are characterized by weaker thermal anomalies. During EP-La Niña, negative anomalies occur mainly in the upper ocean of R2, particularly during DJF(0)–JJA(1), while localized positive anomalies develop intermittently in R1 at intermediate depths. CP-El Niño is dominated by relatively weak negative anomalies in the upper and intermediate ocean, with the clearest cooling occurring in R1 and eastern R2 during DJF(0) and MAM(1). These anomalies weaken substantially in the later stages.

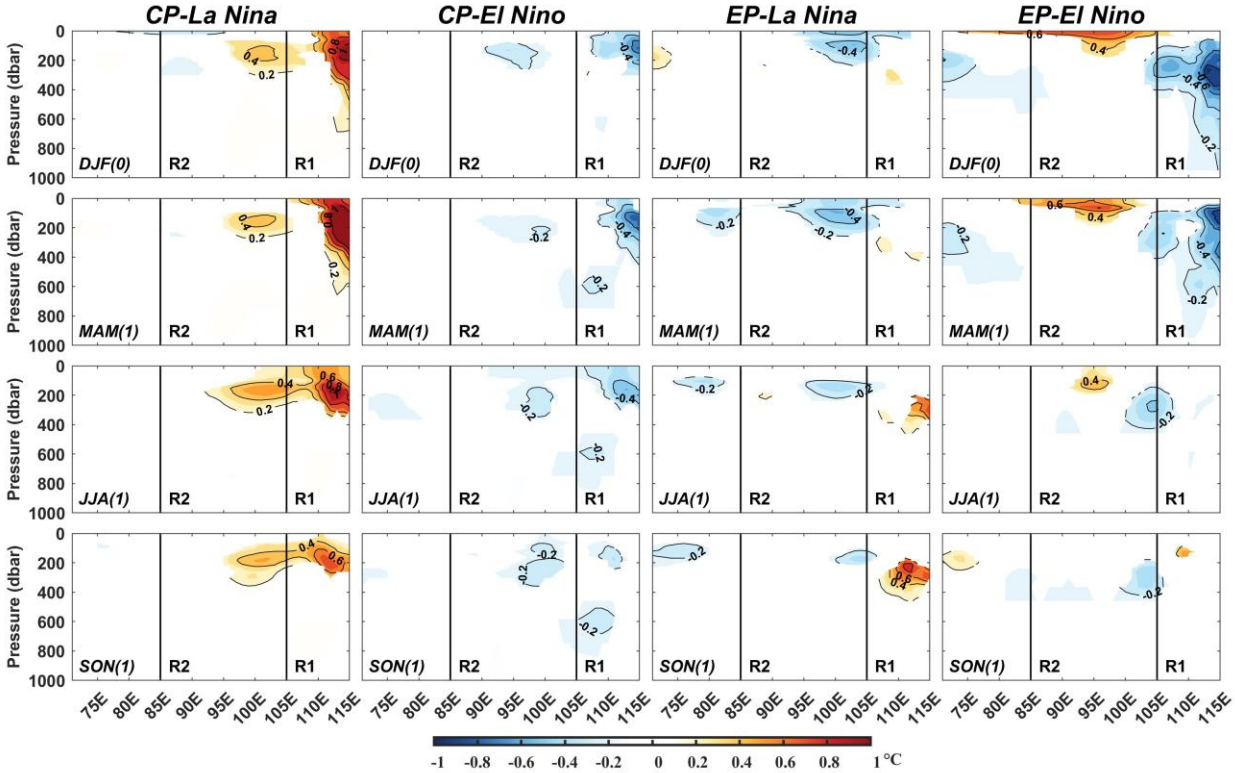


Figure 4. Longitude–pressure sections of composite GODAS temperature anomalies averaged over 20°–35°S during the evolution of four ENSO types: CP-La Niña, CP-El Niño, EP-La Niña, and EP-El Niño. From top to bottom, the rows correspond to DJF(0), MAM(1), JJA(1), and SON(1), where 0 and 1 denote the ENSO developing year and the following year, respectively. Shading and black contours indicate temperature anomalies (°C), with a contour interval of 0.2°C. Only anomalies significant at the 90% confidence level based on a two-sample *t* test against the corresponding all-year sample are shown. The vertical black lines at 85°E and 105°E delineate the regional boundaries, with R2 spanning 85°–105°E and R1 spanning 105°–115°E. Pressure is shown from the surface to 1000 dbar.

The SST composites provide complementary information on the surface expression of these background thermal anomalies (Figure 5). During CP-La Niña, significant positive SSTA are concentrated near the west coast of Australia and gradually fulfill the R1 in MAM(1) and JJA(1). The surface warming remains evident during JJA(1) but weakens markedly by SON(1). A similar near-surface anomaly pattern is reproduced by the 5-m temperature field derived from the GODAS dataset (Figure S1), showing broadly consistent spatial characteristics with the ERSST composite. This consistency rules out the possibility that the differences between the surface and subsurface anomaly distributions can be attributed to the use of different datasets.

During EP-El Niño, significant positive SSTA are distributed mainly across R2 and farther west during DJF(0) and MAM(1), while R1 lacks a persistent and spatially coherent significant warm anomaly. The area of positive SST anomalies decreases during JJA(1) and weakens further by SON(1). This surface distribution is consistent with the strong regional contrast evident in Figure 4: warming occurs predominantly farther west, whereas R1 is characterized by pronounced subsurface cooling at approximately 100–400 dbar. Surface anomalies are comparatively weak during CP-El Niño and EP-La Niña. CP-El Niño shows only localized and spatially discontinuous SST anomalies within the study region. EP-La Niña is characterized primarily by negative SST anomalies across portions of R2 and adjacent waters during DJF(0) and MAM(1), followed by a rapid weakening during JJA(1) and SON(1).

Taken together, Figures 4 and 5 show that ENSO-related thermal variability in the SSIO is both regionally and vertically heterogeneous. CP-La Niña is characterized by persistent warming near the eastern boundary, with the subsurface signal extending farther west than its surface expression. EP-El Niño exhibits a contrasting vertical structure, with pronounced surface warming over a broad portion of the SSIO, including R2, while significant subsurface cooling develops in R1. EP-La Niña broadly resembles the spatial pattern of EP-El Niño but with anomalies of the opposite sign and generally weaker amplitudes. In contrast, CP-El Niño produces only a weak thermal response in R1, with no significant temperature anomalies evident in R2. These contrasts highlight the pronounced asymmetry of the regional thermal response among different ENSO types and phases.

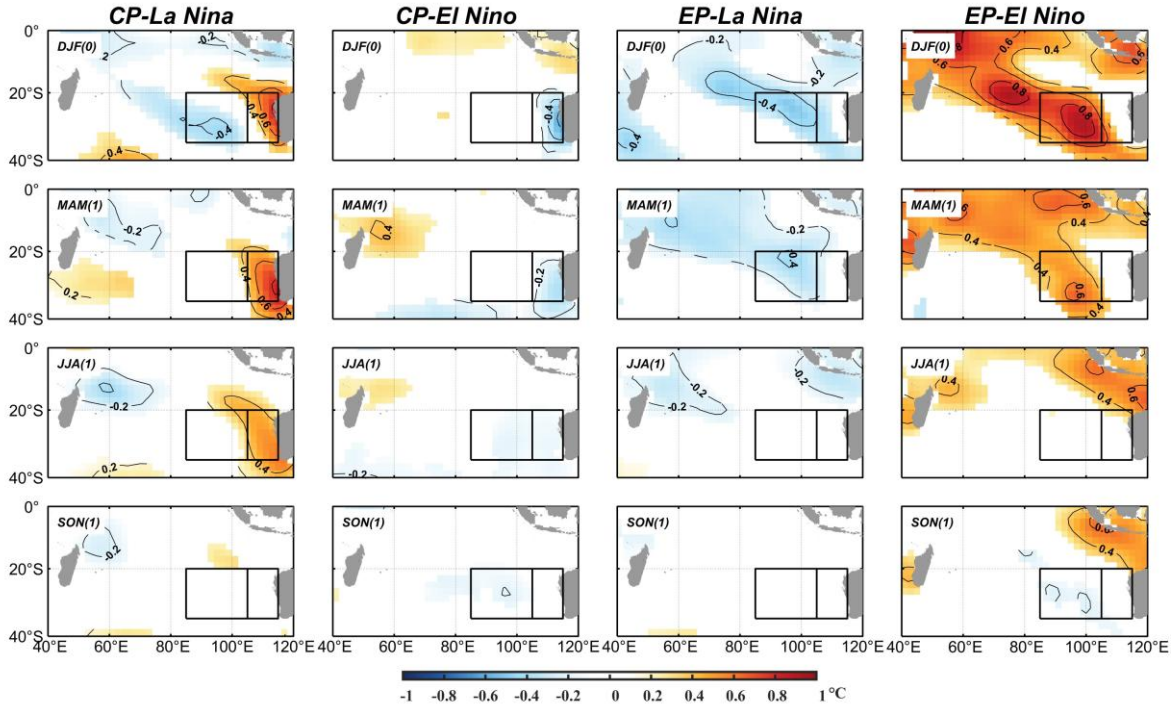


Figure 5. Composite SSTA derived from ERSSTv5 for January 1993-December 2025 during the evolution of four ENSO types in the southeastern Indian Ocean. The four columns from left to right show CP-La Niña, CP-El Niño, EP-La Niña, and EP-El Niño, respectively. The rows from top to bottom correspond to DJF(0), MAM(1), JJA(1), and SON(1), where 0 and 1 denote the ENSO developing year and the following year, respectively. Shading and black contours indicate SST anomalies (°C), with a contour interval of 0.2°C. Only anomalies significant at the 90% confidence level based on a two-sample *t* test against the corresponding all-year sample are shown. Black boxes delineate R1 (105°-115°E, 20°-35°S) and R2 (85°-105°E, 20°-35°S). Gray shading denotes land.

R1 and R2 are embedded in distinct background circulation systems. R1 is influenced primarily by the LC and LUC, with the southward-flowing LC occupying the upper ocean and the northward-flowing LUC beneath it, forming a pronounced vertically opposed meridional circulation. In contrast, R2 is influenced mainly by the SICC and SEC, with the eastward SICC overlying the westward SEC and producing a vertically opposed circulation dominated by the zonal component.

In R1, meridional velocity anomalies show a pronounced vertical structure that varies among ENSO conditions (Figure 6). During CP-La Niña, pronounced negative anomalies are

confined mainly to the upper approximately 0–300 dbar during DJF(0) and MAM(1) and are concentrated toward the western coast of Australia, in agreement with the pattern shown in Figure 4. Positive anomalies emerge below about 400 dbar and become more evident during MAM(1) and JJA(1), resulting in a clear upper–lower sign reversal. During CP-El Niño, positive temperature anomalies dominate the upper ocean during the early stages, with their vertical influence extending to approximately 300 dbar. Negative anomalies are evident below about 300 dbar at intermediate depths. The EP-La Niña response is comparatively weak and spatially fragmented, whereas EP-El Niño exhibits a clearer vertical redistribution, with shallow positive anomalies early in the event followed by more prominent negative anomalies in the upper and intermediate layers. Against this background circulation, the meridional velocity anomalies in Figure 6 provide a dynamical context for the thermal responses shown in Figure 4. During CP-La Niña, the strong southward anomalies in the upper approximately 0–300 dbar reinforce the background LC, favoring enhanced poleward transport of warm tropical waters. This is consistent with the pronounced positive temperature anomalies concentrated near the western coast of Australia in Figure 4. At intermediate depths, the development of northward anomalies is broadly aligned with the background LUC, indicating a simultaneous adjustment of the subsurface circulation. During EP-El Niño, by contrast, the northward anomalies in the upper ocean oppose the background LC during the early stages, implying weakened poleward warm-water transport, consistent with the negative subsurface temperature anomalies observed in R1. These correspondences suggest that ENSO-related modulation of the vertically opposed LC–LUC system contributes to the pronounced vertical thermal variability in R1.

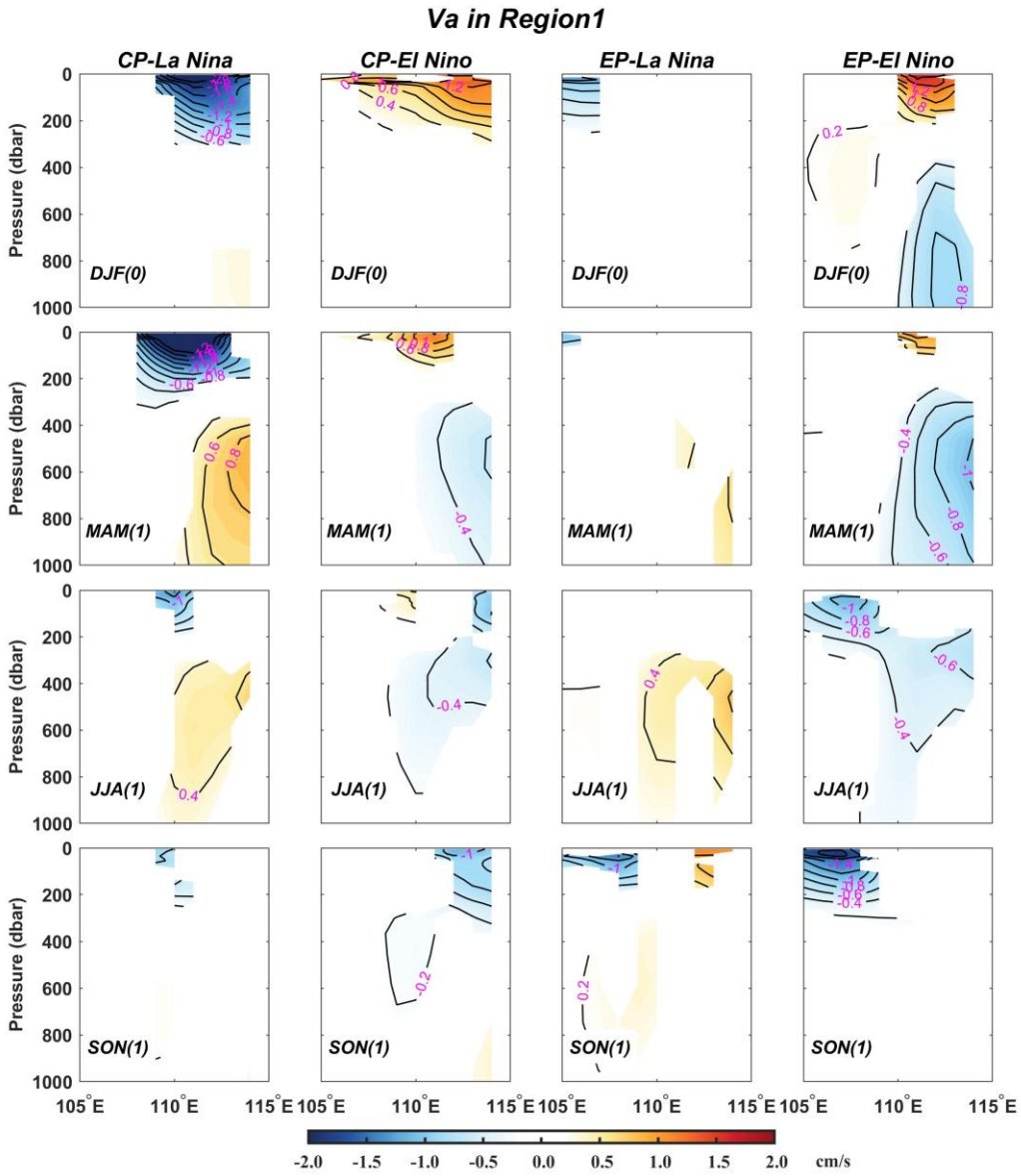


Figure 6. Longitude–depth sections of composite meridional velocity anomalies (Va) in R1; during different ENSO events. From left to right, columns correspond to CP-La Niña, CP-El Niño, EP-La Niña, and EP-El Niño, respectively; from top to bottom, rows represent DJF(0), MAM(1), JJA(1), and SON(1). The meridional velocity is averaged over 35°–20°S. Shading and contours denote velocity anomalies (cm s^{-1}), and only anomalies significant at the 90% confidence level are shown. Positive values indicate northward anomalous flow and negative values indicate southward anomalous flow.

For R2, zonal velocity anomalies are generally weaker and more spatially localized (**Figure 7**). During CP-La Niña, CP-El Niño, and EP-La Niña, significant anomalies are confined mainly

to limited latitude–depth ranges and show relatively weak spatial coherence. In contrast, EP-El Niño produces a clearer R2 response, with negative zonal velocity anomalies concentrated mainly in the northern part of the region and within the upper approximately 200–300 dbar from DJF(0) through JJA(1). Overall, ENSO-related velocity anomalies are expressed more prominently through the meridional component in R1 and the zonal component in R2, providing the circulation background for the vertical-shear analysis presented later.

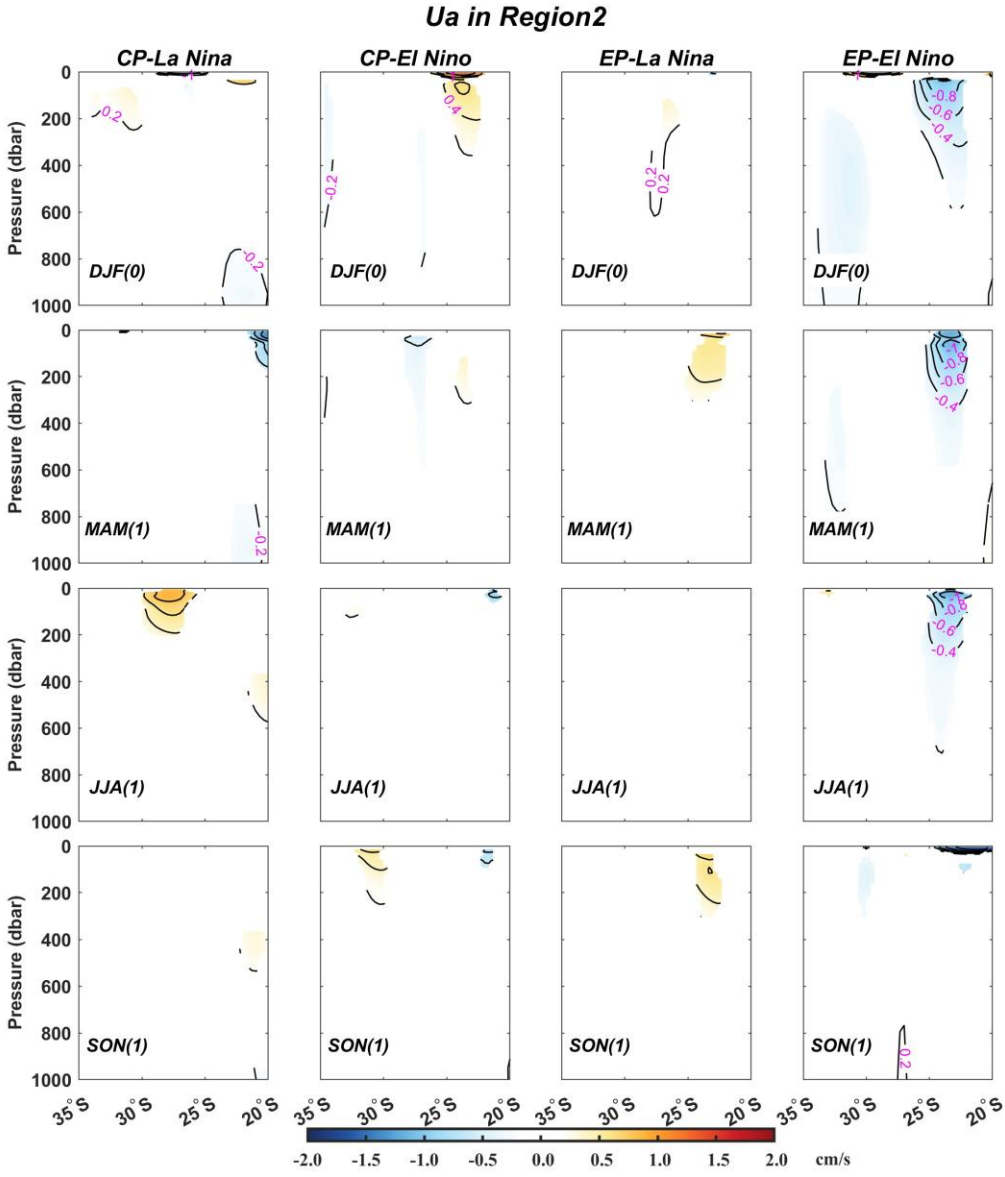


Figure 7. Latitude–depth sections of composite zonal velocity anomalies (Ua) in R2 during different ENSO events. From left to right, columns correspond to CP-La Niña, CP-El Niño, EP-La Niña, and EP-El Niño, respectively; from top to bottom, rows represent DJF(0),

MAM(1), JJA(1), and SON(1). The zonal velocity is averaged over 85°–105°E. Shading and contours denote velocity anomalies (cm s^{-1}), and only anomalies significant at the 90% confidence level are shown. Positive values indicate eastward anomalous flow and negative values indicate westward anomalous flow.

3.2 ENSO-Related Variability in Eddy Activity

Before examining three-dimensional eddy structure, we calculated lead-lag correlations between the EP and CP indices and EKE within eddy interiors (EKE_{AE} and EKE_{CE}; Figure 8). When ENSO leads EKE, the correlations are mostly negative, suggesting that El Niño tends to weaken eddy activity in theSSIO, while La Niña tends to strengthen it,consistent with previous studies (Zheng et al., 2018; Zhang et al., 2020).

The response differs between regions and eddy types. In R1, eddy EKE responds most clearly when ENSO leads by approximately 4-7 months, and CP ENSO has a particularly strong correlation with EKE_{CE} ($r \approx -0.33$). In R2, the correlations extend over longer lead times, especially for CEs. Thus, both EP and CP ENSO affect regional eddy activity, although their effects differ in timing and magnitude.

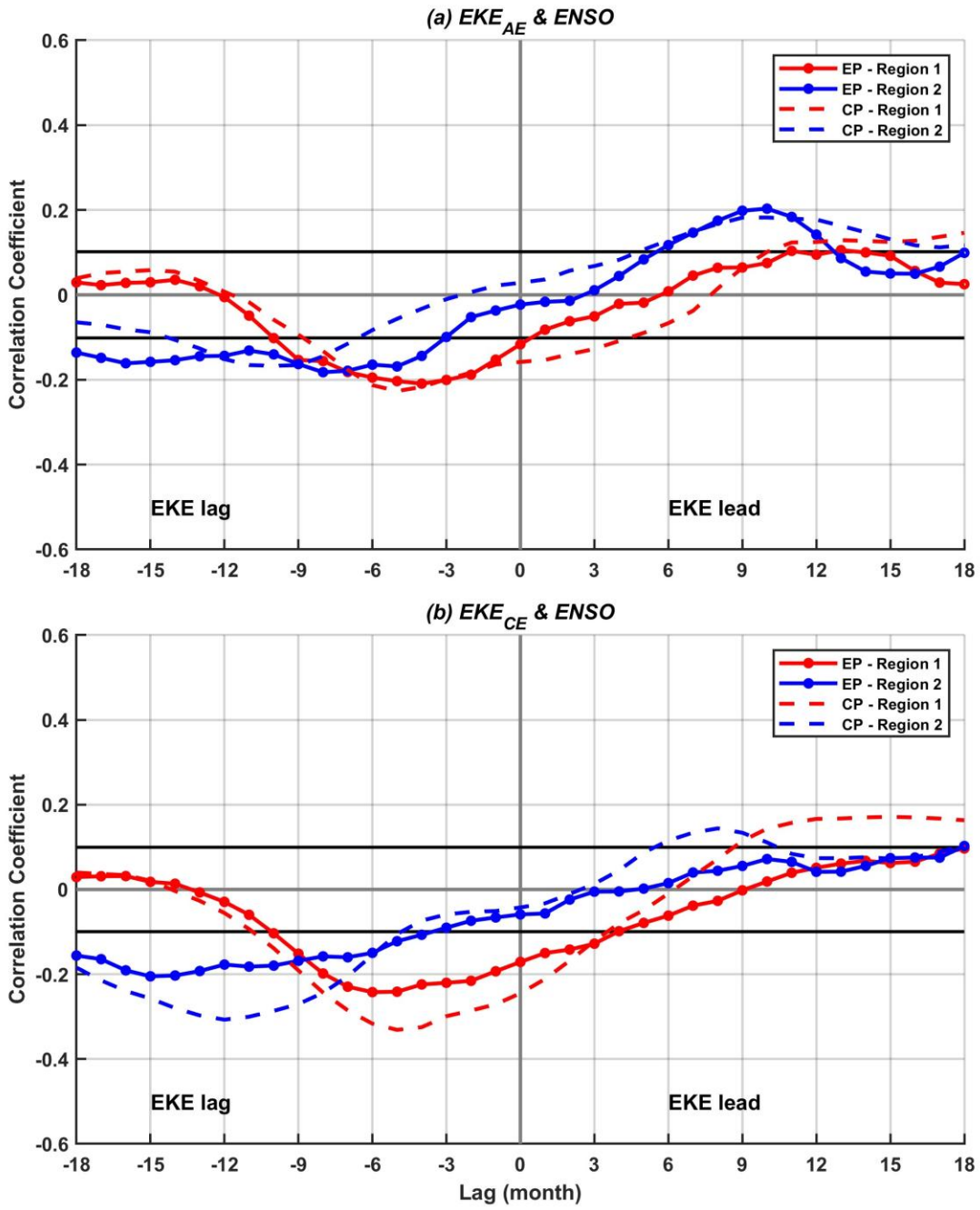


Figure 8. Lead-lag correlations of the EP and CP indices with (a) EKE_{AE} and (b) EKE_{CE} in R1 and R2. Solid and dashed curves represent the EP and CP indices, respectively, while red and blue curves denote Regions 1 and 2, respectively. The black lines indicate the 95% confidence limits. Negative lags denote cases in which the ENSO indices lead EKE.

3.3 Three-Dimensional Eddy Thermal Structure Under EP and CP ENSO

The composite subsurface WOA23-referenced potential temperature anomaly (θ′) fields of R1 AEs show a warm-core structure under all four ENSO conditions (Figure 9), with a particularly clear contrast between CP-La Niña and EP-El Niño. During CP- La Niña, the positive θ′ anomaly is strongest and most vertically coherent, with the main warm core located at approximately 100-500 dbar and extending to about 600 dbar. During EP-El Niño, the upper warm core is weaker and mainly confined to approximately 200-500 dbar, while a secondary positive anomaly appears at around 800-1000 dbar. EP-La Niña also produces a clear warm core at approximately 200–500 dbar, whereas CP-El Niño shows weaker and more vertically separated upper and deeper warm anomalies.

The difference is also evident in the R1 CE composites. During CP-La Niña, a strong positive anomaly above approximately 300 dbar overlies a well-developed cold core extending from about 300 to 900 dbar and centered at approximately 500-700 dbar, forming a distinct warm-over-cold structure. During EP-El Niño, the upper positive anomaly is largely absent, while the subsurface cold core remains prominent. The CP-El Niño and EP-La Niña composites also retain cold cores between approximately 300 and 900 dbar, but their upper-ocean anomalies are generally weak.

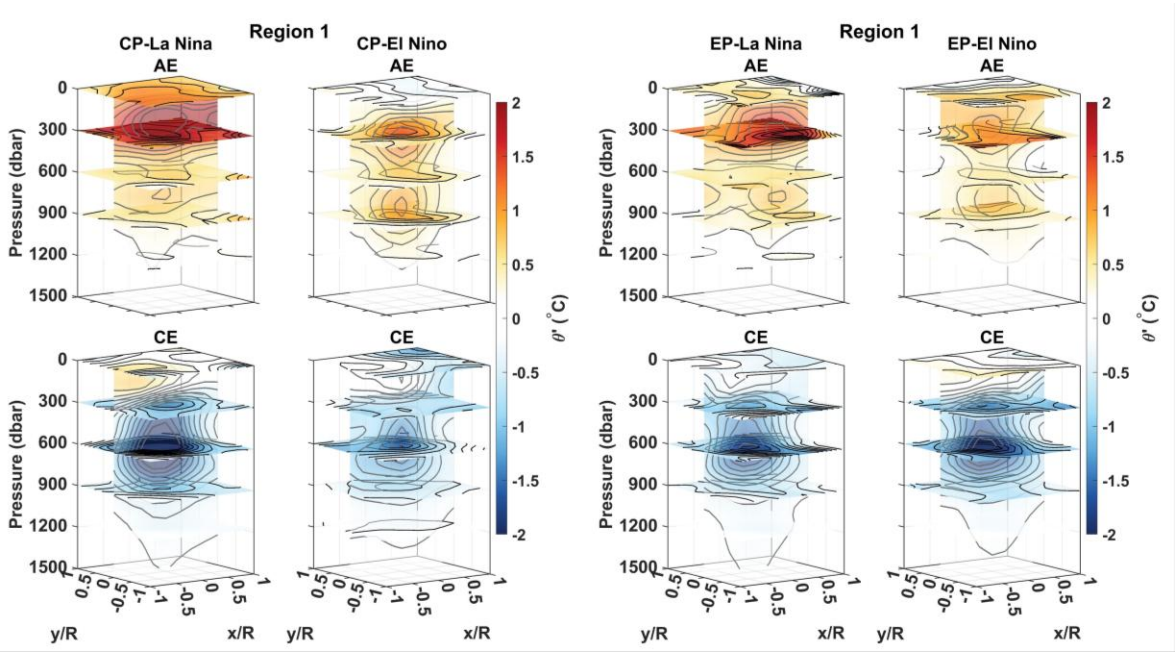


Figure 9. Composite three-dimensional potential temperature anomalies (θ′) within AEs and CEs in R1 (105°-115°E, 20°-35°S) under four ENSO conditions. The left pair of columns

shows CP-La Niña and CP-El Niño, and the right pair shows EP-La Niña and EP-El Niño. The upper and lower rows represent AEs and CEs, respectively. Horizontal sections are shown at 0, 300, 600, 900, 1,200, and 1,500 dbar, together with the vertical section at y/R = 0. Shading and contours indicate θ′ (°C) relative to the WOA23 climatology, with a contour interval of 0.2°C. The x/R and y/R coordinates are distances from the eddy center normalized by eddy radius.

The ENSO-related changes in R2 AEs do not follow the pattern found in R1 (Figure 10). Strong positive θ′ cores occur at approximately 100-500 dbar during both CP-La Niña and EP-El Niño and are comparable in intensity. CP-El Niño also produces a well-defined warm core, although its center is slightly deeper, whereas the anomaly during EP-La Niña is weaker and more diffuse.

A subsurface cold core persists in R2 CEs under all four ENSO conditions, generally extending from about 500 to 1000 dbar and centered at approximately 600-800 dbar. During CP-La Niña, the cold core is strongest and is overlain by a pronounced positive anomaly above about 300 dbar, forming a clear warm-over-cold structure. During EP-El Niño, the subsurface cold core is weaker and the shallow warm anomaly is largely absent. CP-El Niño shows a similar but slightly weaker vertical structure than CP-La Niña, while EP-La Niña represents an intermediate case. The differences among the R2 CE composites are therefore mainly in the strength of the shallow warm and subsurface cold anomalies rather than their depths.

The two regions respond differently to ENSO, and the response also depends on eddy polarity. In R1 AEs, the warm core is strongest during CP-La Niña and weakens during EP-El Niño, whereas R2 AEs have comparably strong warm cores under both conditions. The EP-La Niña and CP-El Niño composites further show that these changes do not follow a simple El Niño–La Niña pattern. For CEs, a subsurface cold core persists in both regions under all four conditions, while the shallow anomaly varies more clearly. CP-La Niña produces the most distinct warm-over-cold structure in both regions. During EP-El Niño, the shallow warming largely disappears; the subsurface cold core remains prominent in R1 but becomes weaker in R2. The main ENSO-related differences therefore lie in the strength and vertical extent of the thermal anomalies rather than in a reversal of the basic eddy structure.

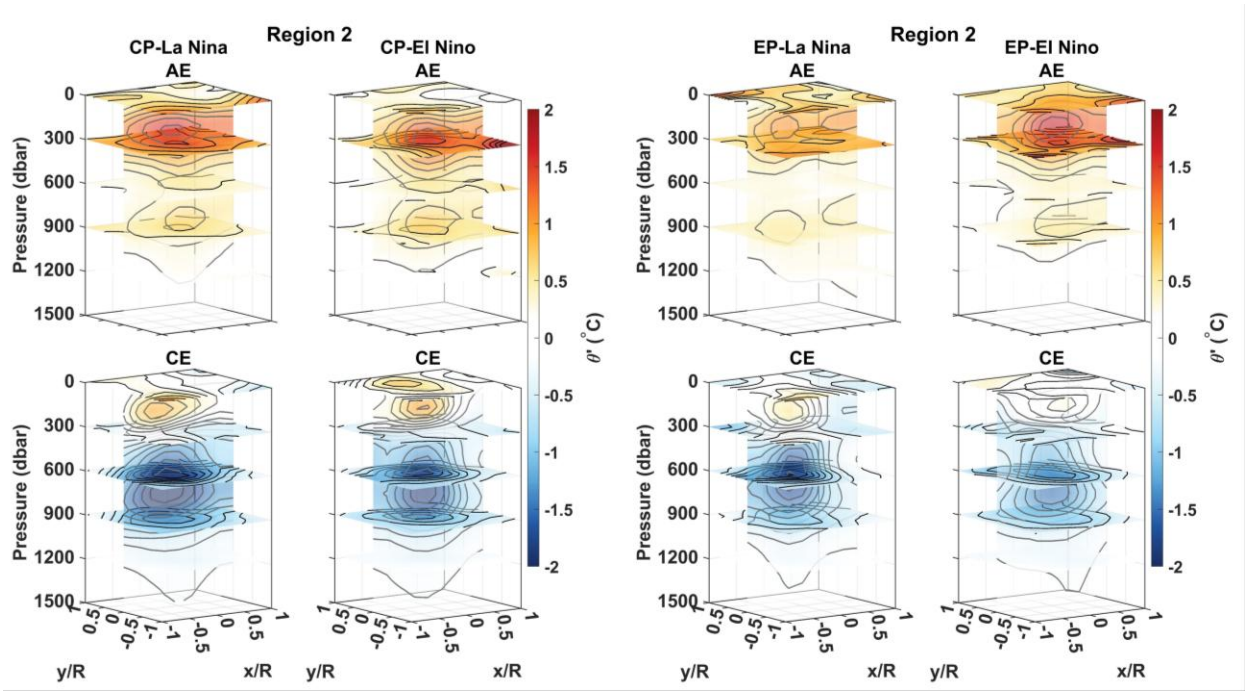


Figure 10. Same as Figure 9, but in R2 (85°-105°E, 20°-35°S).

3.4 Eddy-Induced Thermal Anomalies Relative to Contemporaneous OE Profiles

To assess whether the eddy thermal structures persist after subtracting the contemporaneous environmental background, we compared area-weighted in-eddy potential-temperature profiles with matched OE profiles. In R1, suitable OE matches were found for 562 of 632 CE profiles (88.9%) and 383 of 403 AE profiles (95.0%). In R2, 744 of 875 CE profiles (85.0%) and 788 of 844 AE profiles (93.4%) were matched. Figures 11 and 12 show the resulting eddy-induced potential-temperature anomalies in R1 and R2, respectively. The results are consistent with the basic structures shown in Figures 9 and 10: AEs remain predominantly warm, whereas CEs retain subsurface cold cores under all four ENSO conditions.

In R1, the principal AE warm anomaly occurs at approximately 200–350 dbar and is stronger during CP-La Niña and EP-La Niña but weaker during CP-El Niño. CEs exhibit broad negative anomalies below approximately 250-300 dbar, with cold cores centered near 600-700 dbar. Shallow positive anomalies are also present during CP-La Niña and EP-El Niño (Figure 11).

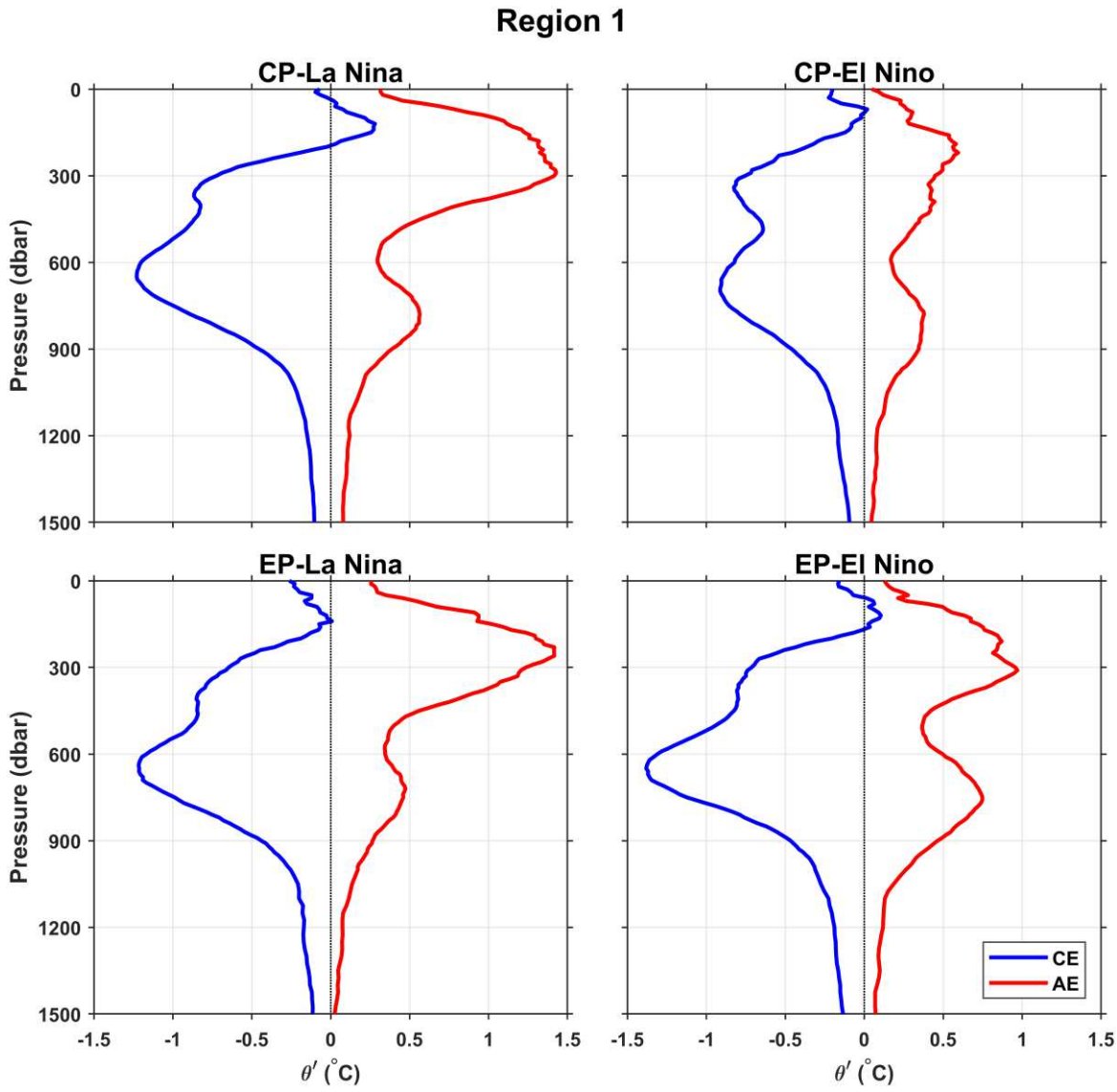


Figure 11. Area-weighted eddy-induced potential-temperature anomaly profiles in R1, defined as the in-eddy profile minus its matched contemporaneous out-of-eddy environmental (OE) reference. Blue and red curves denote CEs and AEs, respectively, and the vertical dotted line denotes zero anomaly. Panels are arranged as CP-La Niña (upper left), CP-El Niño (upper right), EP-La Niña (lower left), and EP-El Niño (lower right). The three radial zones are weighted by 1/9, 3/9, and 5/9 of the eddy area. OE profiles are selected using the sequential time-distance criteria described in Section 2.3. Pressure is shown from 0 to 1,500 dbar.

In R2, the principal AE warm anomaly is concentrated at approximately 150–300 dbar and is relatively weak during EP-La Niña. CEs exhibit shallow warm anomalies overlying subsurface

cold anomalies, with cold cores centered near 650–800 dbar, deeper than those in R1 (Figure 12). This vertical contrast agrees with the regional differences shown in Figures 9 and 10.

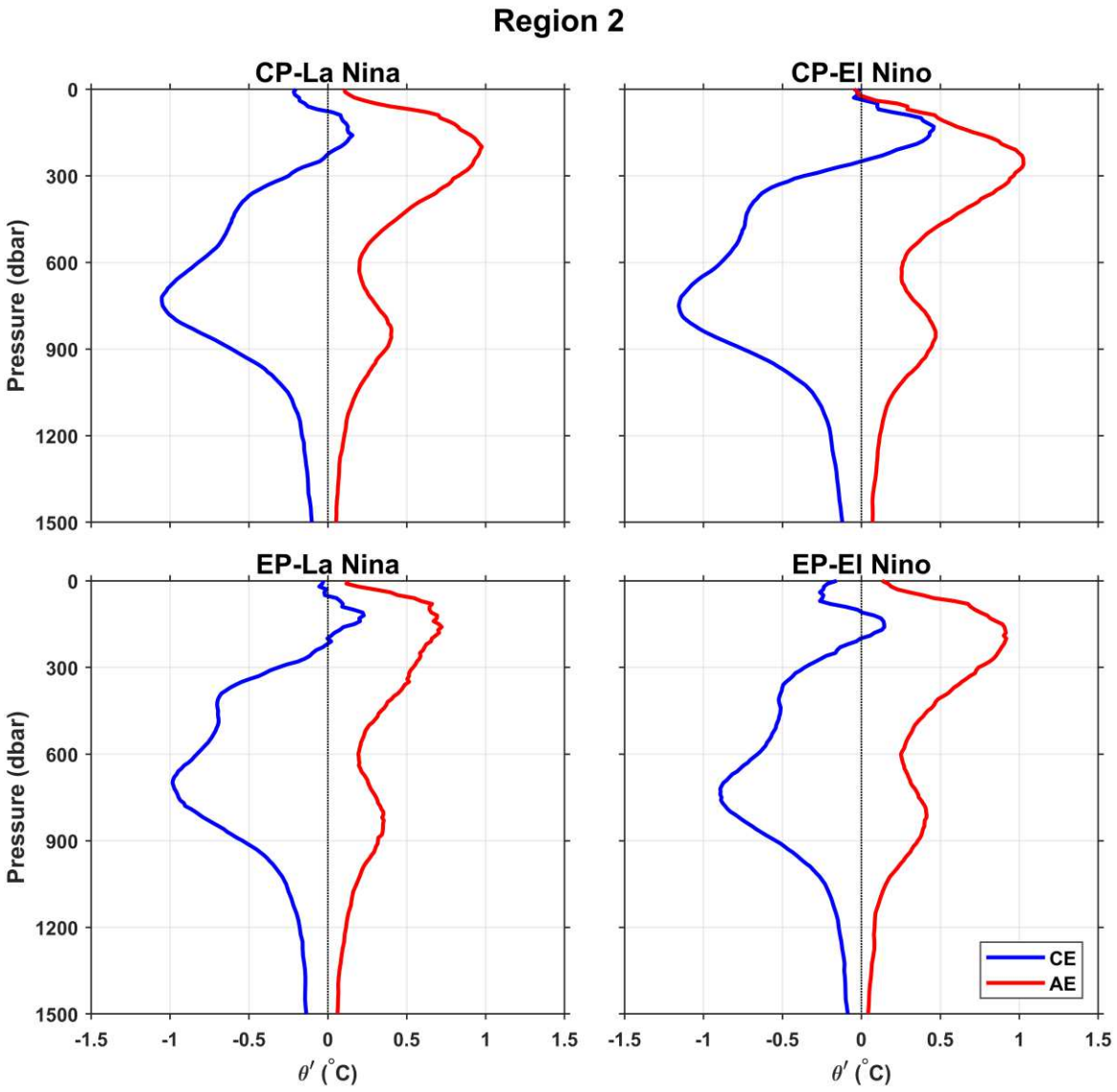


Figure 12. Same as Figure 11, but for R2.

The corresponding in-eddy and OE potential-temperature profiles are presented in Figures S2 and S3. The persistence of AE warm cores, CE subsurface cold cores, and their regional depth differences after subtracting the contemporaneous OE background further supports the thermal structures identified above. Compared with the overall departures from WOA23 climatology, the matched-OE anomalies more directly characterize the temperature contrast between eddies and their surrounding environment under each ENSO condition.

3.5 Eddy Thermal Structure in Relation to ENSO-Related Background Temperature Anomalies

AE warm-core anomalies generally follow the local background temperature pattern, whereas CEs retain a pronounced subsurface cold core under all four ENSO conditions.

3.5.1 Response of AEs to Background Thermal Variability

For AEs, differences among ENSO conditions generally correspond to the local background temperature field, especially in R1 (Figures 4 and 9). During CP-La Niña, R1 exhibits significant and persistent positive background anomalies from the near surface to approximately 300-400 dbar. These anomalies coincide with the strongest and most vertically coherent positive θ' core in AEs, with warming extending to approximately 500–600 dbar. During CP-El Niño, upper- and intermediate-ocean background anomalies in R1 are weak and mainly negative. The upper AE warm core also weakens, while a secondary positive anomaly appears at greater depth. During EP-El Niño, significant negative background anomalies at approximately 100-400 dbar coincide with a marked weakening of the AE warm core in the same depth range.

The R2 results further show that AE structure corresponds more closely to local background structure than to the phase of ENSO alone (Figures 4 and 10). During EP-El Niño, negative upper- and intermediate-ocean anomalies dominate R1, whereas positive anomalies persist in R2. Accordingly, the AE warm core is weak in R1 but remains strong from the near surface to approximately 400 dbar in R2. In R2, the negative upper-ocean background anomalies during EP-La Niña coincide with the weakest AE warm core, while the westward expansion of warm anomalies during CP-La Niña coincides with a strong and coherent warm-core structure. The different AE composites in both regions during the same ENSO event are therefore consistent with regional differences in background temperature.

These regional differences may be related to ENSO-related changes in ocean exchange between the Pacific and Indian Oceans. Sea level anomalies generated in the western Pacific can propagate through the Indonesian seas into the Indian Ocean, altering the Indonesian Throughflow (ITF) and LC system. Zheng et al. (2018) showed that Pacific-origin sea level anomalies strengthen the LC system during La Niña and weaken it during El Niño. Bull et al. (2016) further showed that tropical-source waters constitute an important component of LC transport and that the ITF strongly influences its seasonality. Changes in the Pacific–Indian Ocean exchange and regional heat transport may therefore contribute to the differences in background temperature and AE thermal structure between R1 and R2.

Overall, the AE composites cannot be described simply as weaker during El Niño and stronger during La Niña. Instead, their warm-core anomalies generally follow the local three-dimensional background thermal structure.

3.5.2 Dynamical Modulation of the Subsurface CE Structure

Unlike AEs, CE differences among ENSO conditions correspond less closely to local background temperature anomalies. Under all four ENSO conditions, CEs retain a pronounced subsurface negative θ′ core. This core extends roughly from 300 to 900 dbar in R1 and from 500 to 1000 dbar in R2, with its center located at 600–800 dbar. The main ENSO-related differences occur in the relative strengths of the shallow anomaly and the subsurface cold core.

This persistent subsurface structure is consistent with previous observations of CEs in the LC System. Using satellite and Argo data, He et al. (2021) showed that regional AEs are generally surface intensified, whereas CEs are distinctly subsurface intensified, with a mean density anomaly core near 650 dbar and a deeper temperature anomaly core. Numerical simulations by Rennie et al. (2007) likewise showed that surface LC waters preferentially form surface-intensified warm-core AEs, whereas eddies derived from the LUC are predominantly CEs. Ding et al. (2026) further demonstrated that subsurface-intensified CEs are an important component of the SSIO eddy field and contribute substantially to regional meridional heat transport. These studies emphasize that the subsurface structure is central to CEs dynamic and heat transport. Here, we examine how the CEs' thermal expression changes among different ENSO conditions.

The R1 CE response during CP-La Niña provides the clearest example of the vertical contrast. Background warming is concentrated mainly in the upper 300-400 dbar, while the CE composite shows its strongest positive θ′ in the upper 0-300 dbar. At the same time, a well-developed cold core occupies approximately 500-900 dbar and approaches -2°C near 600 dbar, producing a pronounced warm-over-cold structure. The shallow positive anomaly is consistent with upper-ocean background warming, but the strong cold core below shows that the CE response varies with depth.

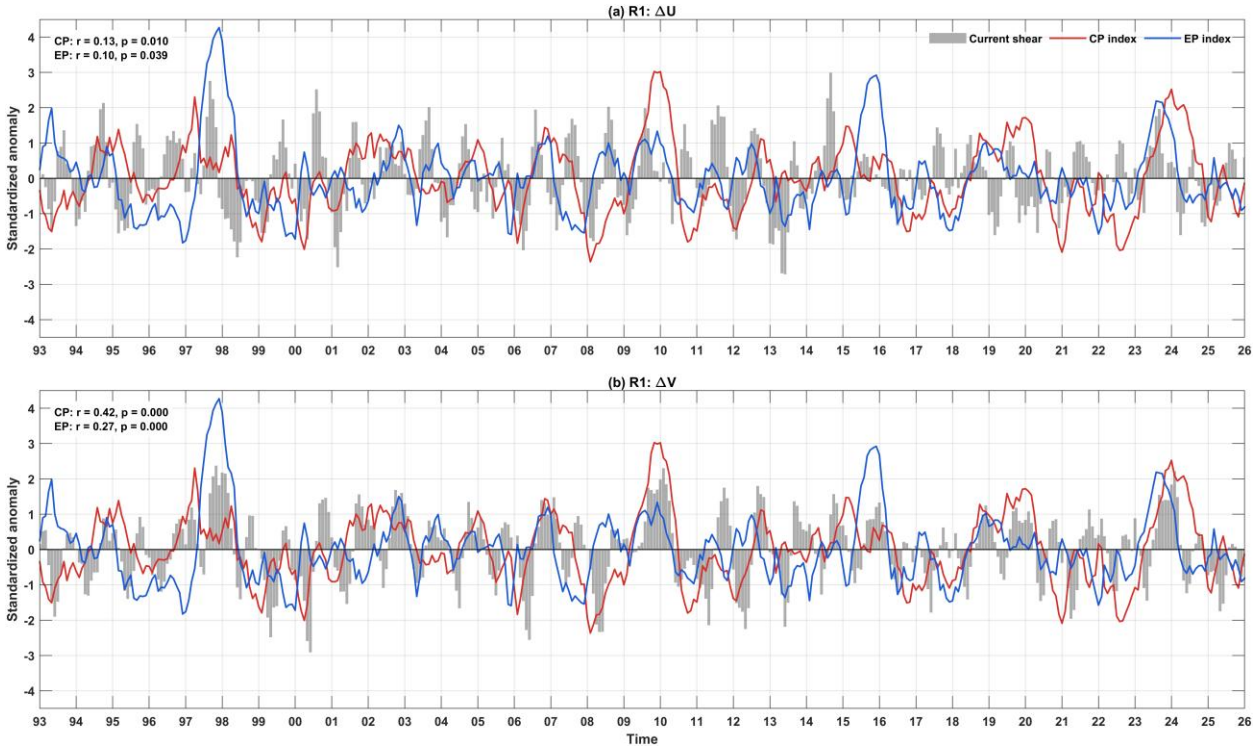


Figure 13. Standardized time series of upper-layer minus lower-layer current shear anomalies in R1 and the CP and EP ENSO indices from January 1993 to December 2025. Gray bars show signed current shear; red and blue curves show the CP and EP indices, respectively. (a) Zonal current shear, defined as $\Delta U = \bar{U}_{0-300} - \bar{U}_{300-1000}$; (b) meridional current shear, defined as $\Delta V = \bar{V}_{0-300} - \bar{V}_{300-1000}$. All time series were standardized after applying an 8-year high-pass filter. The zero-lag Pearson correlation coefficient (r) and corresponding p value between each shear component and the CP and EP indices are shown in each panel. Pressure ranges are in dbar.

The vertical shear analysis (Figure 13) provides further dynamical context. In R1, meridional vertical shear (ΔV) is more strongly correlated with the CP index ($r = 0.42$, $p < 0.001$) than is zonal vertical shear (ΔU; $r = 0.13$, $p = 0.010$). The same difference is found for the EP index, with correlations of $r = 0.27$ ($p < 0.001$) for ΔV and $r = 0.10$ ($p = 0.039$) for ΔU. The stronger relationship with ΔV is consistent with the opposing meridional flows of the poleward upper-layer LC and equatorward lower-layer LUC. Zheng et al. (2018) showed that ENSO can modify eastern-boundary baroclinic instability by altering the meridional vertical shear between the LC and LUC, with shear and EKE increasing during La Niña and decreasing during El Niño. Zhang et al. (2020) also identified baroclinic instability as a major energy source for mesoscale eddy in the SSIO. The

pronounced subsurface cold core in R1 CEs during CP-La Niña may therefore be consistent with changes in LC–LUC vertical shear and the resulting baroclinic instability.

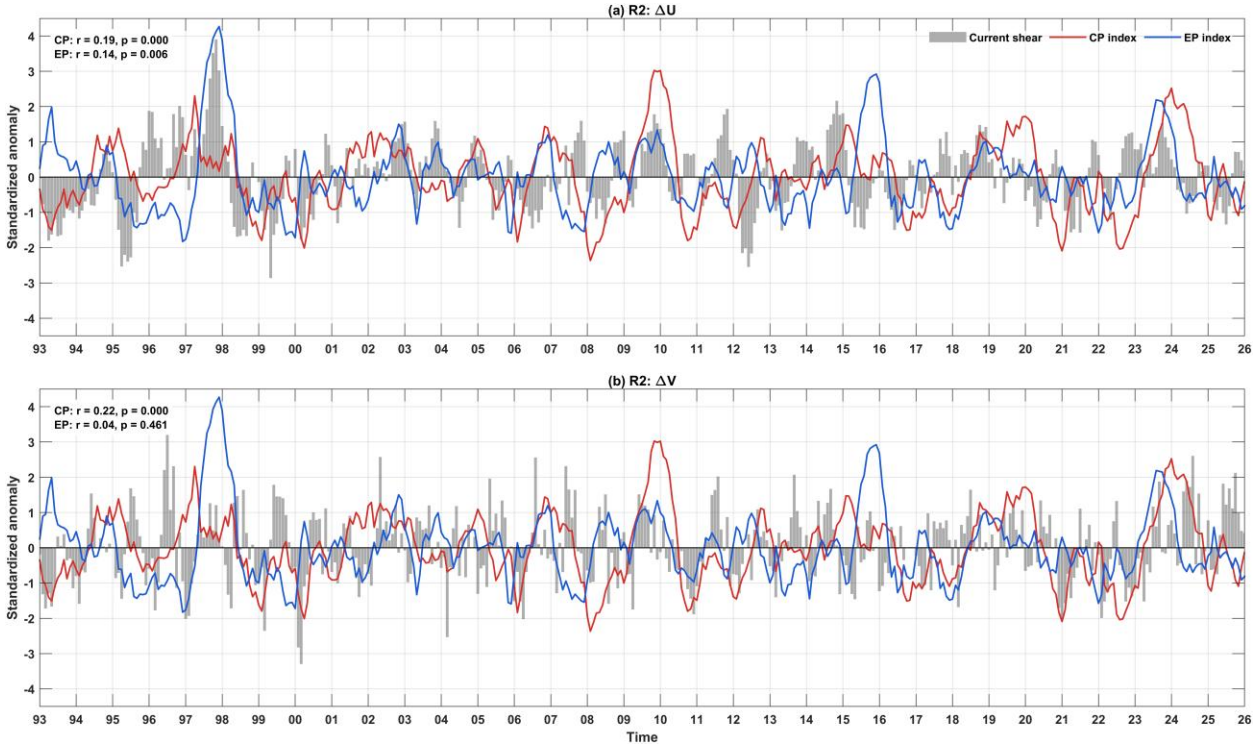


Figure 14. Standardized time series of upper-layer minus lower-layer current shear anomalies in R2 and the CP and EP ENSO indices from January 1993 to December 2025. Gray bars show signed current shear; red and blue curves show the CP and EP indices, respectively. (a) Zonal current shear, defined as $\Delta U = \overline{U}_{0-300} - \overline{U}_{300-1000}$; (b) meridional current shear, defined as $\Delta V = \overline{V}_{0-50} - \overline{V}_{50-1000}$. All time series were standardized after applying an 8-year high-pass filter. The zero-lag Pearson correlation coefficient (r) and corresponding p value between each shear component and the CP and EP indices are shown in each panel. Pressure ranges are in dbar.

R2 CEs likewise retain a persistent cold core at about 500-1000 dbar, but the background shear shows a different directional dependence (Figure 14). In R2, ΔU is significantly correlated with both the CP and EP indices (r = 0.19, p < 0.001; r = 0.14, p = 0.006, respectively). ΔV is also correlated with the CP index (r = 0.22, p < 0.001), but its correlation with the EP index is weak and not significant (r = 0.04, p = 0.461). Unlike R1, where meridional shear is closely related to both ENSO indices, R2 shows a more consistent ENSO signal in zonal shear. Previous studies have identified the zonal shear between the upper eastward SICC and lower westward SEC as an

553 important energy source for baroclinic instability and EKE variability in the interior South Indian
554 Ocean (Jia et al. 2011). Zheng et al. (2018) further linked ENSO-related changes in interior-ocean
555 EKE to SICC-SEC vertical shear. This difference reflects the contrasting background circulation
556 systems in both regions.

557 Trajectory statistics also indicate a possible upstream connection with the eastern
558 boundary. Of the 2,960 AEs and 2,419 CEs generated in R1, 451 AEs and 420 CEs propagate
559 westward into R2, representing 15.2% and 17.4% of the respective totals. The trajectories of eddies
560 with lifetimes of more than 90 days show a distinct westward pathway between the two regions
561 (Figure S4). This pathway agrees with the westward-propagating EKE connection between the LC
562 and SICC systems reported by Zhang et al. (2020). Dilmahamod et al. (2018) also identified long-
563 lived surface and subsurface eddy pathways across the subtropical South Indian Ocean and found
564 that some subsurface eddies retain their water-mass characteristics during westward propagation.
565 Some R2 eddies may therefore retain thermal characteristics acquired farther east while adjusting
566 to the local temperature background field and SICC–SEC shear.

567 Overall, AEs and CEs show two different relationships with ENSO-related background
568 variability. AE warm-core anomalies broadly follow changes in local background temperature.
569 CEs retain a subsurface-intensified structure whose variability corresponds less directly to
570 background warming or cooling. In R1, the ENSO signal is most evident in LC-LUC meridional
571 shear, whereas in R2, SICC-SEC zonal shear is related to both ENSO indices. Westward eddy
572 propagation from R1 may provide an additional connection between the two regions.

573 **4 Summary and Discussion**

574 This study reveals distinct regional and vertical responses of mesoscale eddy thermal
575 structure to EP and CP ENSO in the subtropical southeastern Indian Ocean. By combining satellite
576 altimetry, Argo profiles, and ocean reanalysis, we examine how these responses differ between the
577 eastern sector, Region 1 (R1; 105°-115°E, 20°-35°S), and the central sector, Region 2 (R2; 85°-
578 105°E, 20°-35°S). El Niño generally precedes reduced EKE, whereas La Niña precedes enhanced
579 activity, with region-dependent response times. In R1, the clearest EKE response occurs
580 approximately 4-7 months after ENSO, with a particularly pronounced relationship between CP
581 ENSO and cyclonic eddy activity. In R2, the correlations extend over longer lead times, especially
582 for cyclonic eddies (CEs). These results indicate that ENSO-related eddy variability differs not
583 only in magnitude but also in its temporal expression across the two regions.

The strongest background thermal contrasts occur during CP-La Niña and EP-El Niño. CP-La Niña produces persistent upper-ocean warming in R1, extending to approximately 300-400 dbar, with subsurface warm anomalies extending westward into R2. EP-El Niño instead produces remarkable subsurface cooling at approximately 100-400 dbar in R1 and shallower warming in R2. The background responses during CP-El Niño and EP-La Niña are generally weaker and less spatially coherent. These differences establish distinct thermal environments in which eddies develop and evolve and show that regional ocean responses cannot be represented as a simple reversal between El Niño and La Niña. The contrast between surface and subsurface anomalies also demonstrates that sea surface temperature alone does not fully describe the thermal conditions associated with different ENSO types.

AEs and CEs exhibit different relationships with this background variability. AE warm-core anomalies relative to WOA23 broadly follow local temperature changes. In R1, the warm core is strongest and most vertically coherent during CP-La Niña and weakens during EP-El Niño, consistent with the contrasting background thermal anomalies. In R2, however, comparably strong warm cores occur during both CP-La Niña and EP-El Niño, whereas EP-La Niña produces a weaker and more diffuse anomaly. Thus, the thermal response of AEs depends on the regional background state as well as ENSO type and phase. CEs retain subsurface cold cores across all four ENSO conditions, with the principal differences involving the relative strengths of shallow and subsurface anomalies. CP-La Niña produces the clearest warm-over-cold structure in both regions. During EP-El Niño, the shallow warm anomaly relative to climatology is largely absent, while the subsurface cold core remains prominent in R1 but is weaker in R2. ENSO-related changes therefore primarily modify the strength and vertical expression of the thermal anomalies rather than reverse the basic warm-core or cold-core structure.

Matched-OE composites provides an important complementary assessment of these patterns. After subtracting contemporaneous OE profiles, the principal AE warm cores and CE subsurface cold cores remain evident under all four ENSO conditions. The CE cold cores are centered near 600–700 dbar in R1 and 650–800 dbar in R2, confirming that the regional depth contrast persists when the surrounding thermal environment is taken into account. At the same time, the WOA23-referenced and matched-OE anomalies describe different aspects of eddy thermal variability. The former include both eddy-associated perturbations and environmental departures from climatology, whereas the latter characterize the temperature contrast between

615 eddies and their contemporaneous surroundings. Their agreement on the principal subsurface
616 structures supports the persistence of these features, but does not imply that all shallow anomalies
617 or differences among ENSO categories are independent of the background state. Together, these
618 results extend previous descriptions of eddy vertical structure (He et al. 2021; Ding et al. 2026) by
619 showing how its thermal expression varies with ENSO type, eddy polarity, and regional
620 conditions.

621 Regional differences in vertical shear suggest that ENSO may influence eddy thermal
622 structure through adjustments of the LC–LUC system in R1 and the SICC–SEC system in R2. In
623 R1, both ENSO indices are more strongly related to meridional than zonal vertical shear, consistent
624 with the vertically opposed meridional flows of the LC and LUC. In R2, zonal vertical shear is
625 significantly related to both ENSO indices, whereas the meridional relationship is significant only
626 for the CP index. These contrasting relationships provide a dynamical context for the regional
627 differences in eddy structure and are consistent with previous studies linking vertical shear to
628 baroclinic instability and EKE variability. However, the shear correlations do not directly establish
629 the processes responsible for changes in subsurface cold-core intensity. Diagnosing stratification
630 and energy conversion is necessary to determine how the observed circulation adjustments affect
631 eddy growth and thermal structure.

632 Westward eddy propagation further connects the two regions and suggests that local
633 conditions alone may not account for all thermal variability in R2. Of the eddies generated in R1,
634 451 AEs and 420 CEs subsequently enter R2, representing 15.2% and 17.4% of their respective
635 totals. This connection allows some R2 eddies to carry thermal characteristics acquired farther east
636 while evolving within the local background temperature and SICC-SEC circulation. Nevertheless,
637 the trajectory statistics do not quantify how much of the R2 composite thermal signal is inherited
638 from upstream. Separating locally generated eddies from those arriving from R1, and following
639 their thermal evolution along individual trajectories, would help distinguish these contributions.
640 The coexistence of shallow warming and subsurface cooling also highlights the importance of
641 resolving vertical structure when assessing the potential consequences for ocean heat
642 redistribution. Quantifying those consequences requires velocity–temperature information and
643 transport diagnostics beyond the temperature composites examined here.

644 Several limitations should be considered when interpreting these results. Limited and
645 uneven Argo sampling, together with the relatively small number of events in each ENSO

category, constrains the representation of event-to-event variability. The common composite window facilitates comparison among ENSO categories but may smooth differences in response timing, particularly given the longer EKE response times in R2. Matched-OE subtraction reduces the contribution of the contemporaneous environmental background, although its results remain dependent on the availability and spatial and temporal representativeness of the reference profiles. In addition, the regional GODAS diagnostics describe broad background conditions rather than resolve the instability processes of individual eddies. Other climate modes, including SAM and SIOD, may also contribute to the observed variability; SAM has previously been linked to SICC–SEC shear and EKE changes (Jia et al. 2011). The present analysis does not isolate these influences from those associated with ENSO.

Future work could combine expanded subsurface observations with eddy-resolving model simulations to test whether the regional and vertical contrasts identified here are reproduced across individual events. Event-based resampling and sensitivity tests of the ENSO classification, composite window, and OE matching criteria would help assess the robustness of the inferred differences. Model experiments separating atmospheric and oceanic forcing associated with ENSO and other climate modes could clarify their respective contributions to background temperature, circulation, and eddy variability. Combined analyses of stratification, energy conversion, and individual eddy evolution would then help determine how shear variations influence subsurface cold cores and how thermal structures change during westward propagation. These efforts would provide a firmer basis for connecting ENSO-dependent eddy thermal structure to regional heat redistribution in the subtropical southeastern Indian Ocean.

Data availability

The sea level anomaly (SLA) data used in this study are available from Global Ocean Gridded L4 Sea Surface Heights and Derived Variables Reprocessed 1993 Ongoing (https://doi.org/10.48670/moi-00148). Argo profile data were collected and made freely available by the International Argo Program and the contributing national programs and can be accessed at ftp://ftp.ifremer.fr/ifremer/argo. The World Ocean Atlas 2023 (WOA23), Extended Reconstructed Sea Surface Temperature version 5 (ERSSTv5), and the NCEP Global Ocean Data Assimilation System (GODAS) data are provided by the National Oceanic and Atmospheric Administration (NOAA). WOA23 is available at https://www.ncei.noaa.gov/access/world-ocean-atlas-2023/,

while ERSSTv5 and GODAS data can be accessed through the NOAA Physical Sciences Laboratory at https://psl.noaa.gov/data/.

Author contributions

Chen Fang contributed to the methodology, formal analysis, and writing of the original draft. Guang Yang contributed to conceptualization, supervision, and project administration. Lin Liu was responsible for funding acquisition. Xia Zhao contributed to data curation.

Declarations

Competing interests The authors declare no conflicts of interest relevant to this study.

Acknowledgments

This research was supported by the Basic Scientific Fund for National Public Research Institutes of China (2024Q10), the National Key R&D Program of China (2026YFE0210800), and the National Natural Science Foundation of China (42175027).

Funding

This study was financially supported by the Basic Scientific Fund for National Public Research Institutes of China (2024Q10), the National Key R&D Program of China (2026YFE0210800), and the National Natural Science Foundation of China (42175027).

References

Ari Sadarjoen I, Post FH (2000) Detection, quantification, and tracking of vortices using streamline geometry. Comput Graph 24:333–341. https://doi.org/10.1016/S0097-8493(00)00029-7

Ashok K, Behera SK, Rao SA, et al (2007) El Niño Modoki and its possible teleconnection. J Geophys Res Oceans 112:. https://doi.org/10.1029/2006JC003798

Behringer DW, Xue Y (2004) Evaluation of the global ocean data assimilation system at NCEP: the Pacific Ocean. American Meteorological Society, Seattle, WA

Chaigneau A, Eldin G, Dewitte B (2009) Eddy activity in the four major upwelling systems from satellite altimetry (1992–2007). Prog Oceanogr 83:117–123. https://doi.org/10.1016/j.pocean.2009.07.012

Chaigneau A, Gizolme A, Grados C (2008) Mesoscale eddies off Peru in altimeter records: Identification algorithms and eddy spatio-temporal patterns. Prog Oceanogr 79:106–119. https://doi.org/10.1016/j.pocean.2008.10.013

706 Chaigneau A, Le Texier M, Eldin G, et al (2011) Vertical structure of mesoscale eddies in the
707 eastern South Pacific Ocean: A composite analysis from altimetry and Argo profiling
708 floats. J Geophys Res Oceans 116:. https://doi.org/10.1029/2011JC007134

709 Chelton DB, Schlax MG, Samelson RM (2011) Global observations of nonlinear mesoscale
710 eddies. Prog Oceanogr 91:167–216. https://doi.org/10.1016/j.pocean.2011.01.002

711 Copernicus Marine Service (2025) Global ocean gridded L4 sea surface heights and derived
712 variables reprocessed 1993 ongoing (SEALEVEL_GLO_PHY_L4_MY_008_047)

713 Delman AS, Lee T, Qiu B (2018) Interannual to multidecadal forcing of mesoscale eddy kinetic
714 energy in the subtropical southern Indian Ocean. J Geophys Res Oceans 123:8180–8202.
715 https://doi.org/10.1029/2018JC013945

716 Dilmahamod AF, Aguiar-González B, Penven P, et al (2018) SIDDIES Corridor: A Major East-
717 West Pathway of Long-Lived Surface and Subsurface Eddies Crossing the Subtropical
718 South Indian Ocean. J Geophys Res Oceans 123:5406–5425.
719 https://doi.org/10.1029/2018JC013828

720 Ding W, He Y, Chen Z, et al (2026) Contrasting Structure and Transport Characteristics of
721 Surface- and Subsurface-Intensified Eddies in the Southeastern Indian Ocean. J Geophys
722 Res Oceans 131:e2026JC024296. https://doi.org/10.1029/2026JC024296

723 Eabry MD, Taschetto AS, Maharaj AM, Sen Gupta A (2021) What Determines the Lagged ENSO
724 Response in the South-West Indian Ocean? Geophys Res Lett 48:e2020GL091958.
725 https://doi.org/10.1029/2020GL091958

726 Feng M, Meyers G, Pearce A, Wijffels S (2003) Annual and interannual variations of the Leeuwin
727 Current at 32°S. J Geophys Res Oceans 108:. https://doi.org/10.1029/2002JC001763

728 He Y, Feng M, Xie J, et al (2021) Revisit the Vertical Structure of the Eddies and Eddy-Induced
729 Transport in the Leeuwin Current System. J Geophys Res Oceans 126:e2020JC016556.
730 https://doi.org/10.1029/2020JC016556

731 Huang B, Thorne PW, Banzon VF, et al (2017) Extended reconstructed sea surface temperature
732 version 5 (ERSSTv5): upgrades, validations, and intercomparisons. J Clim 30:8179–8205.
733 https://doi.org/10.1175/JCLI-D-16-0836.1

734 Jia F, Wu L, Lan J, Qiu B (2011) Interannual modulation of eddy kinetic energy in the southeast
735 Indian Ocean by Southern Annular Mode. J Geophys Res Oceans 116:C02029.
736 https://doi.org/10.1029/2010JC006699

737 Jo H-S, Ham Y-G, Kug J-S, et al (2022) Southern Indian Ocean Dipole as a trigger for Central
738 Pacific El Niño since the 2000s. Nat Commun 13:6965. https://doi.org/10.1038/s41467-
739 022-34721-8

740 Kao H-Y, Yu J-Y (2009) Contrasting Eastern-Pacific and Central-Pacific Types of ENSO.
741 https://doi.org/10.1175/2008JCLI2309.1

742 Li J, Clarke AJ (2004) Coastline Direction, Interannual Flow, and the Strong El Niño Currents
743 along Australia's Nearly Zonal Southern Coast. J Phys Oceanogr 34:2373–2381.
744 https://doi.org/10.1175/JPO2645.1

Li Z, Ding R, Mao J, et al (2024) On the Westward Shift and Strengthening of the Atmosphere-To-Ocean Bjerknes Feedback in the Tropical Pacific Since 2000. Geophys Res Lett 51:e2024GL109874. https://doi.org/10.1029/2024GL109874

Liu B, Su Q, Wang H, et al (2023) An Intrathermocline Eddy Observed in the Southeastern Tropical Indian Ocean. Geophys Res Lett 50:e2023GL104462. https://doi.org/10.1029/2023GL104462

Lv M, Wang F, Li Y (2026) Global significance of dipole-pattern SST anomalies in mesoscale eddies. J Phys Oceanogr 56:2275–2287. https://doi.org/10.1175/JPO-D-25-0068.1

Menezes VV, Phillips HE, Schiller A, et al (2014) South I ndian C ountercurrent and associated fronts. J Geophys Res Oceans 119:6763–6791. https://doi.org/10.1002/2014JC010076

Menezes VV, Phillips HE, Vianna ML, Bindoff NL (2016) Interannual variability of the South Indian Countercurrent. J Geophys Res Oceans 121:3465–3487. https://doi.org/10.1002/2015JC011417

National Centers For Environmental Information (2024) World ocean atlas 2023

Nguyen-Le D, Ngo-Duc T, Matsumoto J (2024) The teleconnection of the two types of ENSO and Indian Ocean Dipole on Southeast Asian autumn rainfall anomalies. Clim Dyn 62:1–23. https://doi.org/10.1007/s00382-024-07163-9

Potemra JT (2001) Contribution of equatorial Pacific winds to southern tropical Indian Ocean Rossby waves. J Geophys Res Oceans 106:2407–2422. https://doi.org/10.1029/1999JC000031

Ren H-L, Jin F-F (2011) Niño indices for two types of ENSO. Geophys Res Lett 38:. https://doi.org/10.1029/2010GL046031

Ren H-L, Wang R (2020) Distinct Growth Rates of the Two ENSO Types. Geophys Res Lett 47:e2020GL088179. https://doi.org/10.1029/2020GL088179

Rennie SJ, Pattiaratchi C, Mccauley RD (2007) Eddy formation through the interaction between the Leeuwin Current, Leeuwin Undercurrent and topography. Deep Sea Res Part II Top Stud Oceanogr 54:818–836. https://doi.org/10.1016/j.dsr2.2007.02.005

Schütte F, Brandt P, Karstensen J (2016) Occurrence and characteristics of mesoscale eddies in the tropical northeastern Atlantic Ocean. Ocean Sci 12:663–685. https://doi.org/10.5194/os-12-663-2016

Takahashi K, Montecinos A, Goubanova K, Dewitte B (2011) ENSO regimes: Reinterpreting the canonical and Modoki El Niño. Geophys Res Lett 38:. https://doi.org/10.1029/2011GL047364

Wang Q, Li J (2022) Feedback of tropical cyclones on El Niño diversity. Part I: Phenomenon. Clim Dyn 59:169–184. https://doi.org/10.1007/s00382-021-06122-y

Wang X, Wang C (2014) Different impacts of various El Niño events on the Indian Ocean Dipole. Clim Dyn 42:991–1005. https://doi.org/10.1007/s00382-013-1711-2

Yang G, Liu L, Zhao X, et al (2019a) Impacts of Different Types of ENSO Events on Thermocline Variability in the Southern Tropical Indian Ocean. Geophys Res Lett 46:6775–6785. https://doi.org/10.1029/2019GL082818

Yang G, Yu W, Yuan Y, et al (2015) Characteristics, vertical structures, and heat/salt transports of mesoscale eddies in the southeastern tropical indian ocean. J Geophys Res Oceans 120:6733–6750. https://doi.org/10.1002/2015JC011130

Yang G, Zhao X, Li Y, et al (2019b) Chlorophyll variability induced by mesoscale eddies in the southeastern tropical Indian Ocean. J Mar Syst 199:103209. https://doi.org/10.1016/j.jmarsys.2019.103209

Yit Sen Bull C, van Sebille E (2016) Sources, fate, and pathways of Leeuwin Current water in the Indian Ocean and Great Australian Bight: A Lagrangian study in an eddy-resolving ocean model. J Geophys Res Oceans 121:1626–1639. https://doi.org/10.1002/2015JC011486

Yu J-Y, Kao H-Y, Lee T, Kim ST (2011) Subsurface ocean temperature indices for Central-Pacific and Eastern-Pacific types of El Niño and La Niña events. Theor Appl Climatol 103:337–344. https://doi.org/10.1007/s00704-010-0307-6

Zhang N, Liu G, Liu Q, et al (2020) Spatiotemporal Variations of Mesoscale Eddies in the Southeast Indian Ocean. J Geophys Res Oceans 125:e2019JC015712. https://doi.org/10.1029/2019JC015712

Zhang Y, Fu Y, Zuo B, et al (2025) On the perturbation potential energy in the synergistic effect of ENSO and South China Sea summer monsoon on the Indian Ocean dipole development. Clim Dyn 63:463. https://doi.org/10.1007/s00382-025-07952-w

Zhang Y, Li J, Diao Y, et al (2024) Reconciling roles of the South China Sea summer monsoon and ENSO in prediction of the Indian Ocean dipole. Environ Res Lett 19:014041. https://doi.org/10.1088/1748-9326/ad122a

Zhang Y, Li J, Zheng F, et al (2021) Impact of the South China Sea Summer Monsoon on the Indian Ocean Dipole in CMIP5 Models. J Clim 34:1963–1981. https://doi.org/10.1175/JCLI-D-20-0582.1

Zheng S, Feng M, Du Y, et al (2018) Interannual variability of eddy kinetic energy in the subtropical southeast Indian Ocean associated with the el niño-southern oscillation. J Geophys Res Oceans 123:1048–1061. https://doi.org/10.1002/2017JC013562

Zhu Y, Li Y, Lyu Y, Wang F (2025) Pathways and impacts of ENSO-induced oceanic variability in the southern Indian Ocean investigated with high-resolution model simulations. Deep Sea Res Part Oceanogr Res Pap 222:104532. https://doi.org/10.1016/j.dsr.2025.104532

Zu Y, Fang Y, Sun S, et al (2022) The Seasonality of Mesoscale Eddy Intensity in the Southeastern Tropical Indian Ocean. Front Mar Sci 9:. https://doi.org/10.3389/fmars.2022.855832

Supplementary Files

This is a list of supplementary files associated with this preprint. Click to download.

- SupportingInformation0907.docx